A Region-Specific Ground-Motion Model for Inelastic Spectral Displacement in Northern Italy Considering Spatial Correlation Properties

Chen Huang[1], Karim Tarbali[1], Carmine Galasso[2,*]

[1] Department of Civil, Environmental and Geomatic Engineering, University College London, London, England, UK

[2] Department of Civil, Environmental and Geomatic Engineering, University College London, London, England, UK; also at Scuola Universitaria Superiore (IUSS) Pavia, Pavia, Italy

* Corresponding author: Carmine Galasso

Department of Civil, Environmental and Geomatic Engineering

University College London

London, England, UK WC1E 6BT

Email: c.galasso@ucl.ac.uk

Abstract

The peak inelastic displacement of single-degree-of-freedom bilinear systems (S_{di}) is an effective intensity measure linking ground-motion features to the inelastic response and subsequent structural/nonstructural damage of engineered systems. This study develops a region-specific ground-motion model for S_{di} considering source, path, and site effects and explicitly accounting for the spatial correlation between intraevent residuals when the model parameters are estimated. The model is developed based on 2427 two-component horizontal ground-motion records from 85 events in northern Italy with magnitudes ranging from 4.0 to 6.4 and source-to-site distances less than 200 km. An exponential stationary and isotropic model is considered to represent the spatial correlation properties of S_{di} (after scrutinizing the appropriateness of the underlying assumptions for such a model). Comparisons are performed with existing models in the literature in terms of S_{di} estimates, as well as the (spatial correlation) effective range parameter. Two practical applications of the developed model are presented; one on estimating the spatial distribution of S_{di} (as an essential ingredient for seismic loss assessments); and one on the engineering validation of region-specific ground-motion simulations. Challenges regarding such validations are also discussed.

Introduction

The peak inelastic displacement of single-degree-of-freedom (SDoF) bilinear systems (S_{di}), also referred to as inelastic displacement spectral ordinate, is an effective intensity measure (IM)

relating ground-motion features to the inelastic response and subsequent structural/nonstructural damage of engineered systems (e.g., Stafford *et al.*, 2016). S_{di} can be effectively used (in addition to elastic spectral ordinates) in earthquake-resistant performance-based design (e.g., FEMA 356, 2000; Borzi *et al.*, 2001) and seismic risk assessment (e.g., Raghunandan *et al.*, 2015). In fact, compared to probabilistic seismic demand models using the elastic pseudospectral acceleration at the fundamental period, S_{di} is a more efficient and sufficient ground-motion IM and can reduce the potential bias in the amplitude-scaling of ground motions (e.g., Tothong and Luco, 2007), thus resulting in improved seismic-demand predictions and subsequent damage/loss estimates for multi-degree-of-freedom structures (e.g., O'Reilly *et al.*, 2020). Empirical ground-motion models (GMMs) for S_{di} can provide a direct estimation of the inelastic response of simplified structural systems (e.g., single-degree-of-freedom bilinear systems) based on source, path and site effects (De Luca *et al.*, 2014b, 2014a; Heresi *et al.*, 2018; Akkar and Sandıkkaya, 2019). This is not computationally intensive compared to the rigorous counterpart process (i.e., conducting site-specific seismic hazard analysis based on elastic spectral ordinates; selecting ground-motion time series to represent the hazard; and performing response history analysis on a detailed nonlinear model of the considered system). It is noted that utilizing a single empirical model to circumvent the more rigorous process described above will come with some larger uncertainties in the obtained estimates (that may also be present in the rigorous approach to a certain extent). Moreover, having a GMM for inelastic-response proxies which also incorporates their spatial correlation properties – as proposed in this study – can notably facilitate the performance-based assessment of engineered

52 systems, both for probabilistic seismic hazard analysis as well as scenario-based generation of
53 ground-motion fields (including post-event ShakeMaps).

54 Several GMMs have been developed for S_{di} based on rupture magnitude, focal mechanism,
55 source-to-site distance, and near-surface soil property (to account for source, path, and site effects,
56 respectively) and structural properties (e.g., elastic period, yield strength coefficient, strength-
57 reduction factor, and ductility). Tothong and Cornell (2006) and Stafford *et al.* (2016) proposed
58 empirical GMMs for the inelastic-to-elastic displacement ratios based on the NGA-West (Next
59 Generation of Ground-motion Attenuation) database (Chiou *et al.*, 2008). These models require
60 another GMM (e.g., for elastic spectral ordinates) to estimate the median S_{di} and its variability.
61 De Luca *et al*. (2014a, 2014b), Akkar and Sandıkkaya (2019), and Heresi *et al.* (2018) have directly
62 built GMMs for S_{di} based on Italian, Pan-European and global datasets, respectively. Heresi *et*
63 *al.* (2018) also suggested that utilizing a single GMM (as opposed to a combination of GMMs for
64 the inelastic-to-elastic ratio and elastic spectral ordinates) results in S_{di} estimates characterized
65 by lower uncertainty. More in general, this approach simplifies the two-stage process that requires
66 computing not only the median and standard deviation of the peak elastic displacement and
67 inelastic displacement ratio independently, but also the correlation coefficients between these two
68 random variables.

69 Quantifying the spatial correlation properties of S_{di} is also needed. Various studies (e.g.,
70 Weatherill *et al.*, 2015) have shown that the spatial correlation in ground-motion IMs has important
71 implications on seismic hazard and risk estimates (e.g., earthquake-induced losses) of spatially

distributed engineering systems, such as portfolios of buildings, transportation networks, and other lifelines. The spatial correlation properties of elastic spectral ordinates have been widely investigated (e.g., Goda and Hong, 2008; Jayaram and Baker, 2009; Esposito and Iervolino, 2012; Sgobba *et al.*, 2019, among many others). In this case, it is commonly assumed that the (intraevent) ground-motion residuals follow a Gaussian distribution with zero mean, and their spatial field is a second-order stationary process (i.e., independent of the actual location of the considered sites) and isotropic (i.e., not varying in magnitude according to the considered direction). In contrast to the elastic response, the spatial correlation properties of the inelastic spectral displacement have not been addressed in the literature, and the validity of isotropy and stationarity assumptions has not been examined.

This study aims to fill the abovementioned gaps by developing a region-specific GMM for S_{di} in northern Italy, explicitly accounting for the spatial correlation between intraevent residuals when the model parameters are estimated. Applications of the developed GMM for scenario-based seismic hazard assessment and the engineering validation of simulated ground-motions are presented. Challenges regarding such validations are also discussed.

Case-Study Region and Strong-Motion Database

The ground-motion dataset used by Lanzano *et al.* (2016) to develop an elastic spectral ordinate GMM for northern Italy (hereafter referred to as NI15) is adopted in this study. The strong-motion recordings used in this study are obtained from the Engineering Strong-Motion database

(see Data and Resources). The considered region includes one of the largest alluvial basins in Europe (i.e., the Po Plain area), characterized by moderate seismic hazard (e.g., Stucchi *et al.*, 2011) but associated with a high level of exposure due to the large concentration of industries and critical infrastructures. This has also promoted the development of various physics-based ground-motion simulation methods/applications for the region (e.g., Molinari *et al.*, 2015; Paolucci *et al.*, 2015; Zuccolo *et al.*, 2020, among others), especially following the 2012 Emilia seismic sequence in northern Italy (e.g., Luzi *et al.*, 2013).

Most of the existing GMMs available in the literature (for a variety of IMs) have been derived using recorded data from multiple stations/seismic sources and compiled in global flat files. This has enabled ground-motion modelers to increase the complexity of their models with the aim of reducing epistemic uncertainties (e.g., Gregor *et al.*, 2014; Douglas and Edwards, 2016). However, applying those complex models in practical seismic hazard assessments for specific regions is often a challenging task because of the required input data on the source, path, and site parameters. In addition, ground motions recorded within or at the edge of alluvial basins – as for the case-study region considered here – show very peculiar features (due to the specific propagation effects and local site response), and even more complex GMMs may poorly capture those features. For the specific case of northern Italy, Lanzano *et al.* (2016) demonstrated that region-specific GMMs can outperform complex models developed for larger geographic areas (for example, using global, pan-European, or national datasets) and can lead to a reduction in the hazard levels for several IMs with respect to the values obtained by considering an Italian-wide GMM (Bindi *et al.*, 2011).

111 In this study, a purging process was performed on the initial dataset of Lanzano *et al.* (2016)
112 for the purpose of spatial correlation modeling, including the removal of co-located stations and
113 the removal of events with less than two records classified as free-field motions. The final dataset
114 consists of 2427 two-component pairs of horizontal ground motions recorded at 290 stations in
115 northern Italy during 85 events with a moment magnitude of $4.0 \leq M_W \leq 6.4$, focal depths ≤ 30
116 km, and source-to-site distances (measured by the closest distance to the surface projection of the
117 rupture plane, known as the Joyner-Boore distance, R_{JB}) ≤ 200 km. The geographic
118 distributions of the events and recording stations grouped based on their site classes, according to
119 Eurocode 8 (CEN, 2004), are shown in Figure 1. More details on the considered selection criteria
120 (e.g., the spatial window of the considered events, types of recording stations, and ground-motion
121 processing procedures) can be found in Lanzano *et al.* (2016).
122 Following the NI15 approach, stations belonging to site class C (i.e., with a time-averaged
123 shear-wave velocity at the upper 30 m, V_{S30}, between 180 and 360 m/s) located within the alluvial
124 basins (i.e., in the Po Plain basin or smaller basins in the Apennines) are identified as a special site
125 class C1, with the aim of partially accounting for the presence of surface waves generated due to
126 the basin-edge effect. Lanzano *et al.* (2016) suggested that the ground-motion attenuation in
127 northern Italy depends on the geological domain and source-to-site distance range. Thus, in
128 addition to a hinge distance, an indicator function is considered in NI15 to differentiate the Po
129 Plain basin and the Eastern Alps regions in the north-east (denoted as PEA in the adopted
130 functional form here) from the Northern Apennines region in the south-west (denoted as NA). The

dashed line presented in Figure 1 delineates these two regions. The magnitude-distance scatter plot, and the corresponding histograms are shown in Figure 2. As shown, the considered dataset is dominated by small-to-moderate M_W events (i.e., 80% of the event have $M_W \leq 5.0$ which correspond to 70% of the records); the median source-to-site distance R_{JB} is around 60 km, and 37 % of the records belong to class C1. As shown in Figure 2 (d,e), the PEA and NA datasets are dominated by recordings from site class C1 (i.e., sites of class C within the basin) and site class B, respectively. As the 1976–1977 Friuli and 2012 Emilia sequences (i.e., the two main seismic sequences in the considered dataset, taking up over 60% of the recordings) occurred within the PEA region, the PEA dataset includes more recordings compared to the NA dataset (especially for $R_{JB} \leq 20$ km). It is noted that M_W 6.4 in the PEA region and M_W 6.1 in the NA region are considered as the applicable upper M_W for the developed model.

[Figure 1 about here.]

[Figure 2 about here.]

Peak Inelastic Displacement of Single-Degree-of-Freedom Bilinear Systems

A set of inelastic SDoF oscillators with varying dynamic characteristics are modeled, as follows:

- Elastic vibration period, T_e, ranging between 0.04 and 4 s (36 periods in total);
- Strength reduction factor, R = 2, 4, and 6, defined as the ratio of ground-motion elastic demand to the SDoF system's yield strength (F_y), as shown in Figure 3. R is varied in

order to model the elastic/inelastic structural behavior from elastic $(R = 1)$ SDoF (to investigate also the elastic GMM), to mildly inelastic $(R = 2)$, and severely inelastic structures $(R = 6)$.

- Hysteretic behavior, a non-degrading elastoplastic model with a positive strain-hardening as shown in Figure 3 (with elastic stiffness k and post-elastic stiffness ratio $\alpha_s = 3\%$), representing non-degrading/non-evolutionary SDoF systems.
- A viscous damping coefficient (ζ) of 5%, kept constant throughout the response history analyses.

[Figure 3 about here.]

This simple hysteretic model is chosen as it is conventionally used for assessing the inelastic response of engineered systems for design and assessment purposes (e.g., Priestley, 1997; O'Reilly *et al.*, 2020). Nonlinear dynamic analysis of the considered SDoF oscillators is performed using OpenSees (Mazzoni *et al.*, 2006) by separately subjecting each oscillator to the North-South and East-West components of the records. The geometric mean of the two horizontal components are used in this study to establish the GMM, which also facilitates comparisons with the existing GMMs for S_{di}. The constant-R approach is adopted in this study to ensure that the considered SDoFs will reach consistent levels of nonlinearity (e.g., Galasso *et al.*, 2012). More precisely, for each record, F_y is proportional to the elastic spectral acceleration for that record (at the system's elastic period T_e) divided by the desired R value.

Methodology

GMM functional form

The functional form of NI15 is considered in this study, as presented in Equation (1):

$$y_{ij} = a + F_M(M_W) + F_D(R, M_W) + F_{sof} + F_s + F_{Basin} + \eta_i + \varepsilon_{ij}\ i = 1, \cdots, N, j = 1, \cdots, n_i \quad (1)$$

where

- $y_{ij} = \log_{10} S_{di,ij}$ is the base-10 logarithm of S_{di} (in cm) at station j of event i;
- a is a constant coefficient to be estimated (i.e., the offset of the model);
- $F_M(M_W)$, $F_D(R, M_W)$, F_{sof}, F_s, F_{Basin} are the magnitude scaling, the distance function, the style-of-faulting, the site amplification, and the basin-effects correction, respectively;
- $\boldsymbol{\eta}_i = \eta_i \mathbf{1}_{n_i}$ is the interevent error vector for event $i \in \{1, \dots, N\}$. The $(\eta_i)_{i=1,\dots,N}$ values are independent and identically distributed interevent errors with $\mathbb{E}(\eta_i) = 0$ and $\mathrm{var}(\eta_i) = \tau^2$ for all $i \in \{1, \dots, N\}$ where $\mathbf{1}_{n_i}$ is an $n_i \times 1$ vector of ones;
- $(\boldsymbol{\varepsilon}_i)_{i=1,\dots,N}$ are independent intraevent error vectors of size $n_i \times 1$ with $\mathbb{E}(\boldsymbol{\varepsilon}_i) = \mathbf{0}$ and $\mathrm{cov}(\boldsymbol{\varepsilon}_i) = \phi^2 \boldsymbol{\Omega}_i(\boldsymbol{\omega})$, where $\boldsymbol{\Omega}_i(\boldsymbol{\omega})$ is the spatial correlation matrix corresponding to event i, and $\boldsymbol{\omega}$ is a vector of unknown parameters;
- It is noted that $(\eta_i)_{i=1,\dots,N}$ and $(\boldsymbol{\varepsilon}_i)_{i=1,\dots,N}$ are assumed to be mutually independent; hence, the total standard deviation is calculated as $\sigma = \sqrt{\tau^2 + \phi^2}$ from inter- (τ) and intraevent (ϕ) standard deviations;
- N is the total number of events;

- n_i is the number of recording stations for event i.

The magnitude function is:

$$F_M(M_W) = b_1\left(M_{W,i} - M_r\right) + b_2\left(M_{W,i} - M_r\right)^2, \quad (2)$$

where $M_{W,i}$ is the moment magnitude of event i; M_r is the reference magnitude fixed to 5.0 (following Lanzano *et al.*, 2016); b_1 and b_2 are unknown model parameters. The magnitude saturation has been not considered, because there is no evidence from the data.

The distance function is:

$$F_D(R, M_W) = \left[c_{1k} + c_{2k}\left(M_{W,i} - M_r\right)\right]\log_{10}\left(\frac{R(R_{JB,ij})}{R_h}\right) \quad k = 1, \cdots, 4 \quad (3)$$

where $R(R_{JB,ij}) = \sqrt{R_{JB,ij}^2 + c_3^2}$ with $R_{JB,ij}$ being the Joyner-Boore distance (in kilometers) at station j in event i; c_3 is the fictitious depth to be estimated; $c_{1,2}$ are unknown attenuation coefficients; R_h is the hinge distance fixed to 70 km (following Lanzano *et al.,* 2016), accounting for the changes in the attenuation rate; the index *k* is introduced to account for the dependence of attenuation on the geological domain (i.e., PEA and NA) and distance range, as follows:

$$k = \begin{cases} 1, \text{site located on PEA and } R \le R_h \\ 2, \text{site located on PEA and } R > R_h \\ 3, \text{site located on NA and } R \le R_h \\ 4, \text{site located on NA and } R > R_h \end{cases}. \quad (4)$$

The same indexing is also considered in Lanzano *et al.* (2016).

The style-of-faulting function is:

$$F_{sof} = f_1 F_{N,i} + f_2 F_{T,i} \quad (5)$$

where f_1 and f_2 are unknown model parameters; $F_{N,i}$ and $F_{T,i}$ are dummy variables representing the style of faulting for event i, as:

$$(F_{N,i}, F_{T,i}) = \begin{cases} (0,0)\ Unspecified\ mechanism \\ (1,0)\ Normal\ fault \\ (0,1)\ Thrust\ fault \end{cases} \quad (6)$$

The site amplification is given by

$$F_s = s_1 S_{B,j} + s_2 S_{C,j} \quad (7)$$

where s_1 and s_2 are unknown model parameters; $S_{B,j}$ and $S_{C,j}$ are dummy variables representing the site class according to Eurocode 8 (CEN, 2004) at station j as

$$(S_{B,j}, S_{C,j}) = \begin{cases} (0,0)\ site\ class\ A \\ (1,0)\ site\ class\ B \\ (0,1)\ site\ class\ C \end{cases} \quad (8)$$

Note that site class C1 takes effect in the $I(Basin)$ parameter for basin effects.

The basin-effects correction is defined as,

$$F_{Basin} = \delta_{\text{Basin}} I_j(Basin) \quad (9)$$

where $I(\cdot)$ is an indicator function that equals to one if the condition is met (i.e., whether the station j is in a basin) and zero otherwise; δ_{Basin} is a model parameter to be estimated.

The approach used for regression, including the estimation of the spatial correlation component, is based on the Scoring method developed by Ming *et al.* (2019) and adopted previously by Huang and Galasso (2019) to establish a GMM for peak elastic ground-motion IMs in Italy, and by Huang *et al.* (2020) to establish a GMM for integral ground-motion IMs in Italy. The model parameters, including its coefficients, inter- and intraevent standard deviations, and the range parameter of the spatial correlation model, are obtained in a one-stage maximum likelihood estimation process. Further details on the adopted method can be found in Ming *et al.*, (2019).

Spatial correlation model

Among various options available in the literature (e.g., Rasmussen and Williams, 2006), stationary and isotropic models have been commonly used for representing the spatial correlation properties of earthquake-induced ground motions (e.g., Jayaram and Baker, 2009; Esposito and Iervolino, 2012; Heresi and Miranda, 2019; Huang and Galasso, 2019; Huang *et al.*, 2020). Before choosing an appropriate spatial correlation model for this study, a preliminary GMM without spatial correlation (i.e., the median functional form in Equation 1 with $\boldsymbol{\Omega}_i(\boldsymbol{\omega})$ being the identity matrix) is fitted to examine the assumptions of normality, stationarity, and isotropy for S_{di}. The normality assumption is assessed by the quantile-quantile (QQ) plots of the standardized intraevent S_{di} residuals (i.e., the residuals in log10 unit divided by the estimated standard deviation from the developed model without spatial correlation). The results, not shown here for brevity but available in Figure S1 in the electronic supplement to this article, suggest the assumption of normality is appropriate for the S_{di} residuals. The stationarity and isotropy assumptions are tested based on the Bowman and Crujeiras (2013) approach for each and every event using the *sm* package in the R software environment. The test of stationarity compares the smoothed semivariogram (i.e., an empirical measurement representing the (semi)variance of the difference between two values of a spatially distributed random variable at a given pair of locations) constructed based on location and separation distance bins with its counterpart based only on the separation distance (Bowman and Crujeiras, 2013). In a similar fashion, the test of isotropy compares the smoothed semivariograms over the separation distance and direction of separation vector between two stations with its counterpart smoothed over the separation distance only (Bowman and Crujeiras,

246 2013). The degree of freedom used for smoothing the empirical semivariograms is set to 20 and
247 12 for the tests of stationarity and isotropy, respectively, as recommended by Bowman and
248 Crujeiras (2013). The p-values of the statistical test of stationarity and isotropy are summarized
249 in Figure 4, which shows that the majority of events across the T_e and R values considered in
250 this study have p-values greater than 0.05, indicating that S_{di} generally satisfies the stationarity
251 and isotropy assumptions assuming a 5% significance level.

252 [Figure 4 about here.]

253 The test results for the mainshock of Emilia sequence (the M_W 6.1 2012 May 20 earthquake
254 with the event code IT-2012-0008) are presented in Figure S2 to Figure S4 in the electronic
255 supplement to this article (as an example among the considered events). As shown in those figures,
256 although the smoothed semivariograms show non-stationarity or anisotropy in some cases (as the
257 semivariogram changes over the considered location and direction), the evidence is not statistically
258 significant (as presented in the figure insets by p-values considerably larger than 0.05).
259 Additionally, the isotropy assumption is assessed by the directional semivariograms computed at
260 the orthogonal direction pairs, namely, the fault-normal (FN) and fault-parallel (FP) directions and
261 the 45° and 135° directions[1]. The directional semivariograms are computed at a distance bin of 6
262 km, and each bin contains at least ten pairs of stations. The directional semivariograms (as shown
263 in Figure S5 in the electronic supplement) do not indicate systematic differences across the four

[1] The considered dataset is dominated by events with FN and FP directions close to the 0° and 90°.

considered directions. Based on the general trends in the obtained results, the assumptions of stationarity and isotropy for S_{di} intraevent residuals are retained in this study (although a small number of events showed non-stationarity and/or anisotropy).

Among the available stationary and isotropic models, such as the exponential, squared exponential, and Matérn models (Rasmussen and Williams, 2006), the exponential model presented in Equation 10 has been widely used in the literature because of its appropriate fit to the ground-motion spatial correlation properties (Jayaram and Baker, 2009; Huang and Galasso, 2019; Sgobba *et al.*, 2019; Huang *et al.*, 2020; Kuehn and Abrahamson, 2020):

$$\boldsymbol{\Omega}_{i,jj'}(\boldsymbol{\omega}) = \exp(-\frac{d}{h}) \tag{10}$$

where $\boldsymbol{\Omega}_{i,jj'}(\boldsymbol{\omega})$ is the jj'-th element of the correlation matrix $\boldsymbol{\Omega}_i(\boldsymbol{\omega})$ as a function of unknown parameter $\boldsymbol{\omega}$; h is the range parameter in km indicating the distance at which the correlation is approximately 0.37 (Zimmerman and Stein, 2010); d is the separation distance in km between stations j and j'. The effective range parameter corresponding to 0.05 correlation is computed as $\tilde{h} = 3h$ (Zimmerman and Stein, 2010). Appropriateness of the exponential correlation model is measured based on the Bayesian Information Criteria (BIC) (Schwarz, 1978). The BIC values of the GMM without consideration of spatial correlation in the model estimation, and with exponential, squared exponential, and Matérn correlation models are presented in Table 1. As shown, the exponential model has the lowest BIC values (compared to the model without spatial correlation as well as the other correlation models), which indicates that it provides an appropriate fit to the data.

[Table 1 about here.]

The Developed GMM and Comparisons with Existing Models

The coefficients, standard deviations (total standard deviation σ, interevent standard τ, and intraevent standard deviation ϕ) and the range parameter h of the developed GMM are presented in Table S1 to Table S4 in the electronic supplement to this article.

The median S_{di} spectra and the corresponding 84th and 16th percentiles for a $M_W = 6.0$ thrust event at $R_{JB} = 60$ km (the median distance in the considered dataset) and site classes B and C1 are presented in Figure 5. As shown, the median S_{di} spectra increase as R increases for $T_e < 1.0$s, while the S_{di} spectra for $T_e \geq 1.0$s is similar across different R levels. This is generally expected as the nonlinear behavior of long-period structures broadly follows the empirical equal-displacement rule, while short-period structures generally follow the empirical equal-energy rule (e.g., Chopra, 2007).

[Figure 5 about here.]

Figure 6 presents the median S_{di} predictions and the 16th to 84th percentile ranges for M_W4.5 and M_W6.0 thrust events at site class C1 for two representative T_e and R values in the PEA region. As shown, the median S_{di} from the developed GMM is close to that from De Luca *et al*. (2014a, 2014b) (denoted as D14, hereafter) for $R_{jb} \geq$30 km; however, they deviate more for smaller R_{jb} values. The Akkar and Sandıkkaya (2019) model (denoted as AS19) deviates from the developed GMM at $R_{jb} \geq$5 km for small M_W events and has a different distance attenuation

for large M_W events. The residual analysis of S_{di} for several representative T_e and R (presented in Figure S6 and Figure S7 in the electronic supplement) do not show any notable bias in the proposed GMM with respect to R_{jb}, M_w, focal mechanism, and site class.

[Figure 6 about here.]

The period-dependent total (σ) and intraevent (ϕ) standard deviations from the model are presented in Figure 7 for $R = 1{\sim}6$. As shown, the standard deviations generally reduce as R increase. This can be attributed to the fact that for a highly nonlinear structure, as the secant stiffness of the system decreases (i.e., the effective period increases), the structure is more affected by the long-period ground-motion content, which tends to have lower heterogeneity. The σ values from this study are generally smaller than the Italian D14 model and similar to those from the Pan-European AS19 model. The ϕ values from this study are close to those from AS19 and larger than that from the D14 model. The σ for the elastic spectral displacement from this study (i.e., the $R = 1$ case) is generally similar to that from NI15 at long periods, but higher at short periods due to the consideration of spatial correlation in the developed model, which results in an increase in the estimated ϕ (as discussed in Jayaram and Baker, 2010; Huang and Galasso, 2019; Ming *et al.*, 2019).

[Figure 7 about here.]

In terms of spatial correlation properties, Figure 8 shows the effective range parameters $\tilde{h}$ as a function of T_e for three inelasticity values. The $\tilde{h}$ values from other models for elastic spectral ordinates are also presented for comparison, namely, Huang and Galasso (2019), Sgobba *et al.*

(2019), and Schiappapietra and Douglas (2020) (denoted as SLP19, HG19, and SD20, respectively). It is noted that, to the best of the authors' knowledge, the spatial correlation properties for inelastic responses have not been addressed in the literature. Figure 8 shows that the $\tilde{h}$ values are larger for long periods due to the lower spatial variation of long-period ground-motion characteristics. The results also show that the $\tilde{h}$ values for the inelastic systems (i.e., $R > 1$) are generally similar across different R values. The $\tilde{h}$ values for the elastic ordinates from this study (i.e., $R = 1$ case) are higher at short periods than those of SLP19 (developed specifically for the Po Plain region) and vice versa at long periods. Both this study and SLP19 result in larger $\tilde{h}$ values when compared to the HG19 and SD20 models (developed based on the data from the entire Italian territory, and central Italy, respectively). Considering that both the SLP19 model and this study use the NI15 functional form, the observed differences may come from the regional and event-specific variations in the ground-motion spatial properties (Jayaram and Baker, 2009; Huang *et al.*, 2020; Schiappapietra and Douglas, 2020). It is noted that the national and central Italian databases are dominated by events from normal faults, whereas the northern Italy database is dominated by events from reverse faults. Also, the spatial correlation modeling approach (i.e., the empirical semivariogram approach of SLP19 versus the one-stage scoring estimation approach of Ming *et al.* (2019) utilized here) may contribute to these differences. Finally, the SLP19 model uses the non-ergodic approach to model ground-motion variability, whereas this study uses the more conventional inter- and intra-event residual decomposition.

[Figure 8 about here.]

Applications

The developed GMM can be utilized to generate S_{di} estimates for the purpose of seismic design and loss assessments, as discussed above. Figure 9 presents an example of such applications for a M_W 6.0 thrust event in the Po Plain region. For both plots in Figure 9, a realization of S_{di} is generated for a system with $T_e = 2.0s$ and $R = 2$ by considering the median and standard deviation for the event. However, Figure 9a also considers the spatial correlation properties of S_{di} based on the developed model. As shown, Figure 9a presents a reasonable spatial realization of S_{di} as opposed to a totally random characteristics in Figure 9b, which may have important implications in assessing seismic damage and resulting losses for spatially distributed engineered systems. For long-period S_{di}, the corresponding range parameters h (and effective range parameter $\tilde{h}$) characterizing the spatial correlation are similar across different R levels as illustrated in Figure 8 and Table S1-S4 in the electronic supplement to this article. Thus, the scenarios for other R levels are not shown here for brevity.

[Figure 9 about here.]

The developed model can also be used for the engineering validation of ground motions simulated in the region of interest for this study. In fact, recent advances in high-performance computing and understanding of complex seismic source features, as well as path and site effects, have led to increasing research efforts and development in physics-based ground-motion simulations. Today, physics-based simulated (or "synthetic") ground motions represent a valuable supplement to recorded ground motions for several practical applications (e.g., scenario-based and

363 probabilistic seismic hazard analysis, performance-based earthquake engineering). Among
364 engineers and risk modelers, the general concern is that simulated ground motions may not be
365 equivalently valid when compared with real records in estimating seismic demands, damage, and
366 loss to engineered systems. A significant amount of research has been conducted in recent years to
367 validate ground-motion simulation methods for engineering applications (e.g., Galasso *et al.*, 2012,
368 2013; Burks and Baker, 2014; Bradley *et al.*, 2017, among many others). Various researchers (e.g.,
369 Star *et al.*, 2011; Dreger *et al.*, 2015) have also performed statistical comparisons of ground
370 motions from hybrid ground-motion simulations to GMMs for various IMs (e.g., Star *et al.*, 2011;
371 Afshari and Stewart, 2016; Lee *et al.*, 2019).

372 To demonstrate an application of the GMM developed in this study for S_{di}, a physics-based
373 ground-motion simulation of the M_W 6.0 (29 May 2012) Emilia-Romagna earthquake, Italy, is
374 considered for illustrative purposes (Paolucci *et al.*, 2015). The S_{di} field from the simulated
375 ground motions for a system with $T_e = 2.0s$ and $R = 2$ is shown in Figure 10. The low-
376 frequency ground motions of this simulation are generated based on the spectral element method
377 using the SPEED package (Mazzieri *et al.*, 2013). The resulting simulations are then combined
378 with high-frequency ground motions by correlating the high-frequency content to the simulated
379 low-frequency ground motions. This is done using the artificial neural networks approach of
380 Paolucci *et al.* (2018). Then, the broadband ground motions are obtained by merging the high- and
381 low-frequency contents at the frequency of 1.5Hz. It is noted that the low-frequency ground
382 motions (applicable for frequencies up to about 1.5Hz) have been previously validated in terms of

383 elastic engineering demands against recordings and empirical GMMs (Paolucci *et al.*, 2015), and
384 a generally good agreement has been found between the simulated and recorded motion in both
385 time and frequency domains, especially for the horizontal North-South and the vertical component.
386 It is worth pointing out that the intent here is to discuss the application of the developed GMM
387 for ground-motion simulation validation purposes rather than providing a definitive judgment on
388 this specific simulation method(s)/simulated ground motions.
389 [Figure 10 about here.]
390 Specifically, the ratio of S_{di} from the simulation over the median S_{di} from the considered
391 GMM is calculated using Eq. (5):
392 $$\text{ratio} = \log_{10}\left(\frac{S_{di,Sim}}{S_{di,GMM}}\right). \quad (5)$$
393 Figure 11 presents this ratio for 21 stations (e.g., T0813 and MRN stations, among others, as
394 in Figure 10) of the considered simulation. As shown, the S_{di} values from the simulation are
395 generally smaller than the median S_{di} values from the proposed GMM (as also shown in Figure
396 10). In the absence of recorded ground motions, one cannot discern whether the simulation results
397 are not an appropriate representation of the reality, or the utilized GMM is not well-constrained
398 for the region and the event of interest (in terms of the rupture and velocity structure
399 characteristics). To further investigate the difference between the considered simulations and the
400 proposed GMM, comparisons should be made with the existing observed ground motions. Figure
401 11 shows such a comparison based on the ratio calculated using Eq. (6) for the simulation and
402 developed GMM with respect to the recorded ground motions:

$$\text{ratio} = \log_{10}\left(\frac{S_{di,Sim} \text{ or } S_{di,GMM}}{S_{di,Rec}}\right). \quad (6)$$

As shown in Figure 11, the S_{di} values from the simulations are unbiased (close to the ratio of zero in MRN and T0813 stations, for example) in the vicinity of the rupture plane ($R_{JB} \leq 8$ km), especially for long periods; however, they are generally underestimating the recorded motions at larger distances. The S_{di} values from the developed GMM is generally similar to that from the records in stations with $R_{JB} \leq 20$ as the zero-ratio line is generally within the 16th-84th percentile ratios of the developed GMM. This is broadly expected as the records from this event are within the dataset used to develop the GMM. However, this event is at the tail of the M_w distribution considered in the study (see Figure 2). The empirical GMM overestimates the S_{di} in comparison to the records for $R_{JB} > 20$ km.

[Figure 11 about here.]

These comparisons clearly show some limitations of conducting validation based on empirical GMMs. However, this approach for comparison/validation could be the only possible approach to use when simulations are done for future events or for regions with little or no strong-motion recordings. It is noted that such validations for future events should be conducted using GMMs that are well-constrained for the event and the region of interest (because the GMM themselves might not represent the region-specific ground-motion properties for a potential future event).

Conclusions

This study developed a region-specific ground-motion model including its spatial correlation

properties for inelastic spectral displacement (S_{di}) in northern Italy. This model provides a direct estimation of S_{di} based on the source, path, and site parameters and can be utilized in the seismic performance-based assessment of engineered systems, both for probabilistic seismic hazard analysis as well as scenario-based generation of ground-motion fields (including post-event ShakeMaps). An exponential function was utilized for the purpose of spatial correlation modeling based on statistical tests on the validity of isotropy and stationarity assumptions. Comparisons with the recent Italian and European models were performed, and the differences in terms of the model standard deviations, distance attenuation, and effective range parameter were discussed. The results indicated that the effective range parameter is similar across the various inelasticity levels, and close to that from the elastic spectral ordinates for long periods. Application of the developed model for validating simulated ground motions highlighted that the empirical GMMs utilized as the benchmark model in validation should be well-constrained for the event and region of interest, as well as for the source-to-site distance and ground-motion content (i.e., vibration period) of interest.

Data and Resources

The strong-motion recordings used in this study are available from the Engineering Strong-Motion database http://esm.mi.ingv.it (last accessed July 2020). The nonparametric tests of stationarity and isotropy are implemented by sm package in R environment. The one-stage estimation algorithm is available at https://github.com/mingdeyu/GMPE-estimation (last accessed July 2020). An

electronic supplement is prepared for this article, which includes the model parameters of the developed GMM with spatial correlation for elastic (R=1) and three inelasticity levels (R=2, 4, and 6), the supplementary test results of the assumptions of normality, stationarity and isotropy, and the residual analysis.

Acknowledgments

This study is funded by the China Scholarships Council (grant number 201608440273) for Chen Huang, and by the "Dipartimenti di Eccellenza" project by the Italian Ministry of Education, University and Research at IUSS Pavia for Carmine Galasso. The authors would like to thank Prof. Roberto Paolucci, Dr Chiara Smerzini, and Dr Iario Mazzieri at Politecnico di Milano, Italy, for sharing the simulated ground motions for the Emilia-Romagna earthquakes. The authors also acknowledge the insightful comments from Prof. Julian Bommer (Imperial College London) and an anonymous reviewer, that improved the quality of this study.

References

Afshari, K., and J. P. Stewart (2016). Validation of duration parameters from SCEC broadband platform simulated ground motions, *Seismol. Res. Lett.* **87**, no. 6, 1355–1362, doi: 10.1785/0220160086.

Akkar, S., and M. A. Sandıkkaya (2019). A ground motion model to estimate nonlinear deformation demands from a recent Pan European strong motion database, in *2019 Society for Earthquake and Civil Engineering Dynamics (SECED) conference*, Greenwich, London,

UK, 9-10th September.

Bindi, D., F. Pacor, L. Luzi, R. Puglia, M. Massa, G. Ameri, and R. Paolucci (2011). Ground motion prediction equations derived from the Italian strong motion database, *Bull. Earthq. Eng.* **9**, no. 6, 1899–1920, doi: 10.1007/s10518-011-9313-z.

Borzi, B., G. M. Calvi, A. S. Elnashai, E. Faccioli, and J. J. Bommer (2001). Inelastic spectra for displacement-based seismic design, *Soil Dyn. Earthq. Eng.* **21**, no. 1, 47–61, doi: 10.1016/S0267-7261(00)00075-0.

Bowman, A. W., and R. M. Crujeiras (2013). Inference for variograms, *Comput. Stat. Data Anal.* **66**, 19–31, doi: 10.1016/j.csda.2013.02.027.

Bradley, B. A., D. Pettinga, J. W. Baker, and J. Fraser (2017). Guidance on the utilization of earthquake-induced ground motion simulations in engineering practice, *Earthq. Spectra* **33**, no. 3, 809–835, doi: 10.1193/120216EQS219EP.

Burks, L. S., and J. W. Baker (2014). Validation of ground-motion simulations through simple proxies for the response of engineered systems, *Bull. Seismol. Soc. Am.* **104**, no. 4, 1930–1946, doi: 10.1785/0120130276.

CEN (2004). *Eurocode 8 : Design of structures for earthquake resistance - Part 1: General rules, seismic actions and rules for buildings*, European Committee for Standardization, Brussels, Belgium, p. 232.

Chiou, B. S. J., R. Darragh, N. Gregor, and W. J. Silva (2008). NGA project strong-motion database, *Earthq. Spectra* **24**, no. 1, 23–44, doi: 10.1193/1.2894831.

480 Chopra, A. (2007). *Dynamics of Structures - Theory and Applications to Earthquake Engineering,*
481 Pearson Prentice-Hall, Upper Saddle River, N.J., pp. 876.
482 De Luca, F., G. Ameri, I. Iervolino, F. Pacor, and D. Bindi (2014a). Toward validation of simulated
483 accelerograms via prediction equations for nonlinear SDOF response, *Boll. di Geofis. Teor.*
484 *ed Appl.* **55**, no. 1, 85–101, doi: 10.4430/bgta0114.
485 De Luca, F., G. Ameri, I. Iervolino, F. Pacor, and D. Bindi (2014b). Erratum to Toward validation
486 of simulated accelerograms via prediction equations for nonlinear SDOF response (Bollettino
487 di Geofisica Teorica ed Applicata (2014) 55 (81-101)), *Boll. di Geofis. Teor. ed Appl*. **55**, no.
488 4, 789.
489 Douglas, J., and B. Edwards (2016). Recent and future developments in earthquake ground motion
490 estimation, *Earth-Science Rev.* **160**, 203–219, doi: 10.1016/j.earscirev.2016.07.005.
491 Dreger, D. S., G. C. Beroza, S. M. Day, C. A. Goulet, T. H. Jordan, P. A. Spudich, and J. P. Stewart
492 (2015). Validation of the SCEC broadband platform v14.3 simulation methods using
493 pseudospectral acceleration data, *Seismol. Res. Lett.* **86**, no. 1, 39–47, doi:
494 10.1785/0220140118.
495 Esposito, S., and I. Iervolino (2012). Spatial correlation of spectral acceleration in European data,
496 *Bull. Seismol. Soc. Am.* **102**, no. 6, 2781–2788, doi: 10.1785/0120120068.
497 FEMA 356 (2000). *Prestandard and Commentary for the Seismic Rehabilitation of Buildings*,
498 Federal Emergency Management Agency, Washington, D.C., p. 518.
499 Galasso, C., F. Zareian, I. Iervolino, and R. W. Graves (2012). Validation of ground-motion

simulations for historical events using SDoF systems, *Bull. Seismol. Soc. Am.* **102**, no. 6, 2727–2740, doi: 10.1785/0120120018.

Galasso, C., P. Zhong, F. Zareian, I. Iervolino, and R. W. Graves (2013). Validation of ground-motion simulations for historical events using MDoF systems, *Earthq. Eng. Struct. Dyn.* **42**, 1395–1412, doi: 10.1002/eqe.2278.

Goda, K., and H. P. Hong (2008). Spatial correlation of peak ground motions and response spectra, *Bull. Seismol. Soc. Am.* **98**, no. 1, 354–365, doi: 10.1785/0120070078.

Gregor, N., N. A. Abrahamson, G. M. Atkinson, D. M. Boore, Y. Bozorgnia, K. W. Campbell, B. S. J. Chiou, I. M. Idriss, R. Kamai, E. Seyhan, *et al.* (2014). Comparison of NGA-West2 GMPEs, *Earthq. Spectra* **30**, no. 3, 1179–1197, doi: 10.1193/070113EQS186M.

Heresi, P., H. Dávalos, and E. Miranda (2018). Ground motion prediction model for the peak inelastic displacement of single-degree-of-freedom bilinear systems, *Earthq. Spectra* **34**, no. 3, 1177–1199, doi: 10.1193/061517EQS118M.

Heresi, P., and E. Miranda (2019). Uncertainty in intraevent spatial correlation of elastic pseudo-acceleration spectral ordinates, *Bull. Earthq. Eng.* **17**, no. 3, 1099–1115, doi: 10.1007/s10518-018-0506-6.

Huang, C., and C. Galasso (2019). Ground-motion intensity measure correlations observed in Italian strong-motion records, *Earthq. Eng. Struct. Dyn.* **48**, no. 15, 1634–1660, doi: 10.1002/eqe.3216.

Huang, C., K. Tarbali, and C. Galasso (2020). Correlation properties of integral ground-motion

intensity measures from Italian strong-motion records, *Earthq. Eng. Struct. Dyn.*, doi: 10.1002/eqe.3318.

Jayaram, N., and J. W. Baker (2009). Correlation model for spatially distributed ground-motion intensities, *Earthq. Eng. Struct. Dyn.* **38**, no. 15, 1687–1708, doi: 10.1002/eqe.922.

Jayaram, N., and J. W. Baker (2010). Considering spatial correlation in mixed-effects regression and the impact on ground-motion models, *Bull. Seismol. Soc. Am.* **100**, no. 6, 3295–3303, doi: 10.1785/0120090366.

Kuehn, N. M., and N. A. Abrahamson (2020). Spatial correlations of ground motion for non-ergodic seismic hazard analysis, *Earthq. Eng. Struct. Dyn.* **49**, no. 1, 4–23, doi: 10.1002/eqe.3221.

Lanzano, G., M. D'Amico, C. Felicetta, R. Puglia, L. Luzi, F. Pacor, and D. Bindi (2016). Ground-motion prediction equations for region-specific probabilistic seismic-hazard analysis, *Bull. Seismol. Soc. Am.* **106**, no. 1, 73–92, doi: 10.1785/0120150096.

Lee, R., B. A. Bradley, P. J. Stafford, R. W. Graves, and A. Rodriguez-marek (2019). Hybrid broadband ground motion simulation validation of small magnitude earthquakes in Canterbury, New Zealand, *Earthq. Spectra* **DOI:10.117**, doi: 10.1177/8755293019891718.

Luzi, L., F. Pacor, G. Ameri, R. Puglia, P. Burrato, M. Massa, P. Augliera, G. Franceschina, S. Lovati, and R. Castro (2013). Overview on the strong-motion data recorded during the May-June 2012 Emilia seismic sequence, *Seismol. Res. Lett.* **84**, no. 4, 629–644, doi: 10.1785/0220120154.

Mazzieri, I., M. Stupazzini, R. Guidotti, and C. Smerzini (2013). SPEED: SPectral Elements in Elastodynamics with Discontinuous Galerkin: a non-conforming approach for 3D multi-scale problems, *Int. J. Numer. Methods Eng.* **95**, 991–1010, doi: 10.1002/nme.4532.

Mazzoni, S., F. McKenna, M. H. Scott, and G. L. Fenves (2006). *Open System for Earthquake Engineering Simulation (OpenSEES) User Command-Language Manual*, Pacific Earthquake Engineering Research Center, California, p.465.

Ming, D., C. Huang, G. W. Peters, and C. Galasso (2019). An advanced estimation algorithm for ground-motion models with spatial correlation, *Bull. Seismol. Soc. Am.* **109**, no. 2, 541–566, doi: 10.1785/0120180215.

Molinari, I., A. Argnani, A. Morelli, and P. Basini (2015). Development and testing of a 3D seismic velocity model of the Po Plain sedimentary basin, Italy, *Bull. Seismol. Soc. Am.* **105**, no. 2, 753–764, doi: 10.1785/0120140204.

O'Reilly, G. J., R. Monteiro, A. M. B. Nafeh, T. J. Sullivan, and G. M. Calvi (2020). Displacement-based framework for simplified seismic loss assessment, *J. Earthq. Eng.* **24**, no. sup1, 1–22, doi: 10.1080/13632469.2020.1730272.

Paolucci, R., F. Gatti, M. Infantino, C. Smerzini, A. Güney Özcebe, and M. Stupazzini (2018). Broadband ground motions from 3D physics-based numerical simulations using artificial neural networks, *Bull. Seismol. Soc. Am.* **108**, no. 3A, 1272–1286, doi: 10.1785/0120170293.

Paolucci, R., I. Mazzieri, and C. Smerzini (2015). Anatomy of strong ground motion: Near-source records and three-dimensional physics-based numerical simulations of the Mw 6.0 2012 may

29 po plain earthquake, Italy, *Geophys. J. Int.* **203**, no. 3, 2001–2020, doi: 10.1093/gji/ggv405.

Priestley, M. J. N., 1997. Displacement-based seismic assessment of reinforced concrete buildings, *J. Earthq. Eng.* **1**, no. 1, 157-192, doi: 10.1080/13632469708962365.

Raghunandan, M., A. B. Liel, and N. Luco (2015). Collapse risk of buildings in the pacific northwest region due to subduction earthquakes, *Earthq. Spectra* **31**, no. 4, 2087–2115, doi: 10.1193/012114EQS011M.

Rasmussen, C. E., and C. K. I. Williams (2006). *Gaussian processes for machine learning*, MIT Press, Cambridge, MA, p. 248.

Schiappapietra, E., and J. Douglas (2020). Modelling the spatial correlation of earthquake ground motion: Insights from the literature, data from the 2016–2017 Central Italy earthquake sequence and ground-motion simulations, *Earth-Science Rev.* **203**, no. 103139, doi: 10.1016/j.earscirev.2020.103139.

Schwarz, G. (1978). Estimating the dimension of a model, *Ann. Stat.* **6**, no. 2, 461–464, doi: 10.1214/aos/1176344136.

Sgobba, S., G. Lanzano, F. Pacor, R. Puglia, M. D'amico, C. Felicetta, and L. Luzi (2019). Spatial correlation model of systematic site and path effects for ground-motion fields in northern Italy, *Bull. Seismol. Soc. Am.* **109**, no. 4, 1419–1434, doi: 10.1785/0120180209.

Stafford, P. J., T. J. Sullivan, and D. Pennucci (2016). Empirical correlation between inelastic and elastic spectral displacement demands, *Earthq. Spectra* **32**, no. 3, 1419–1448, doi: 10.1193/020515EQS021M.

Star, L. M., J. P. Stewart, and R. W. Graves (2011). Comparison of ground motions from hybrid simulations to nga prediction equations, *Earthq. Spectra* **27**, no. 2, 331–350, doi: 10.1193/1.3583644.

Stucchi, M., C. Meletti, V. Montaldo, H. Crowley, G. M. Calvi, and E. Boschi (2011). Seismic hazard assessment (2003-2009) for the Italian building code, *Bull. Seismol. Soc. Am.* **101**, no. 4, 1885–1911, doi: 10.1785/0120100130.

Tothong, P., and C. A. Cornell (2006). An empirical ground-motion attenuation relation for inelastic spectral displacement, *Bull. Seismol. Soc. Am.* **96**, no. 6, 2146–2164, doi: 10.1785/0120060018.

Tothong, P., and N. Luco (2007). Probabilistic seismic demand analysis using advanced ground motion intensity measures, *Earthq. Eng. Struct. Dyn.* **36**, no. 13, 1837–1860, doi: 10.1002/eqe.696.

Weatherill, G. A., V. Silva, H. Crowley, and P. Bazzurro (2015). Exploring the impact of spatial correlations and uncertainties for portfolio analysis in probabilistic seismic loss estimation, *Bull. Earthq. Eng.* **13**, no. 4, 957–981, doi: 10.1007/s10518-015-9730-5.

Zimmerman, D. L., and M. Stein (2010). Classical Geostatistical Methods, in *Handbook of spatial statistics* A. E. Gelfand, P. J. Diggle, M. Fuentes, and P. Guttopr(Editors), CRC Press, 29–44.

Zuccolo, E., F. Bozzoni, J. Crempien, and C. G. Lai (2020). Nonlinear broadband simulation of the Mw 6.0 May 29, 2012 Emilia earthquake in Northern Italy, *Soil Dyn. Earthq. Eng.* **129**, 105931, doi: 10.1016/j.soildyn.2019.105931.

600

Author Mailing Addresses

Chen Huang

Department of Civil, Environmental and Geomatic Engineering

University College London

London, England, UK WC1E 6BT

Email: chen.huang.14@ucl.ac.uk

Karim Tarbali

Department of Civil, Environmental and Geomatic Engineering

University College London

London, England, UK WC1E 6BT

Email: k.tarbali@ucl.ac.uk

Carmine Galasso

Department of Civil, Environmental and Geomatic Engineering

University College London

London, England, UK WC1E 6BT

Email: c.galasso@ucl.ac.uk

Tables

Table 1 BIC values of the candidate spatial correlation models

Spatial	$\boldsymbol{R = 2}$			$\boldsymbol{R = 4}$		
correlation model	$\boldsymbol{T_e = 0.5s}$	$\boldsymbol{T_e = 1.0s}$	$\boldsymbol{T_e = 2.0s}$	$\boldsymbol{T_e = 0.5s}$	$\boldsymbol{T_e = 1.0s}$	$\boldsymbol{T_e = 2.0s}$
None	874	855	929	835	820	921
Exponential	663	323	245	552	389	280
Squared exponential	882	862	937	843	824	928
Matérn	882	862	916	829	828	908

List of Figure Captions

Figures

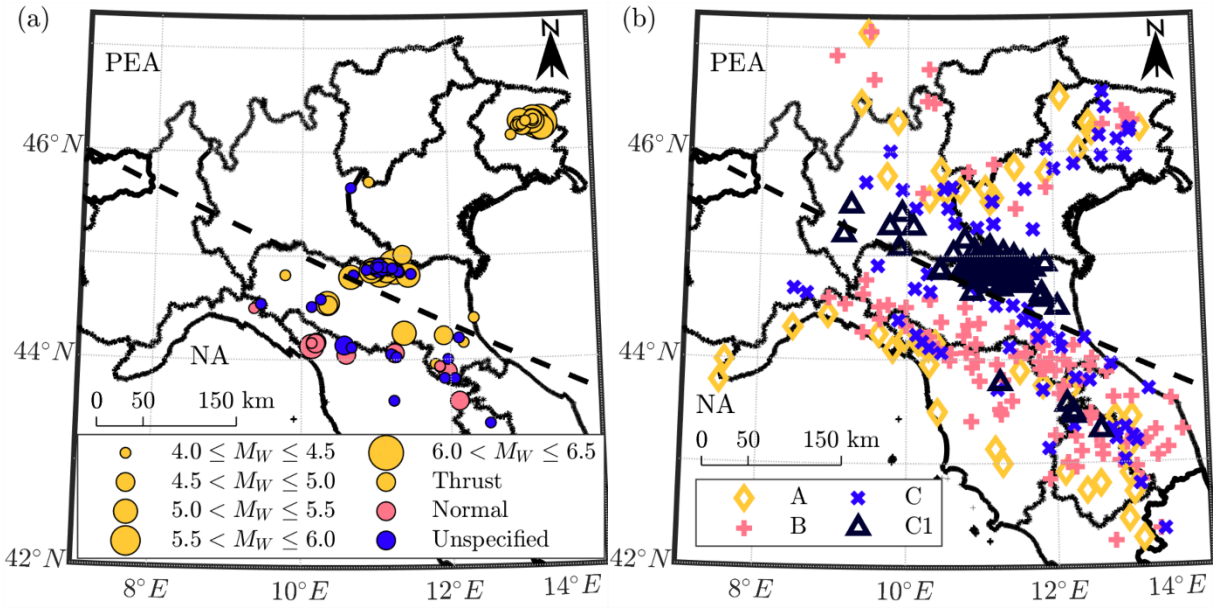

Figure 1 Geographic distributions of the considered events (a) grouped based on their M_W and focal mechanism; and stations (b) grouped by their site classes. The dashed line delineates the Po Plain basin and Eastern Alps regions (denoted as PEA) from the Northern Apennines region (denoted as NA).

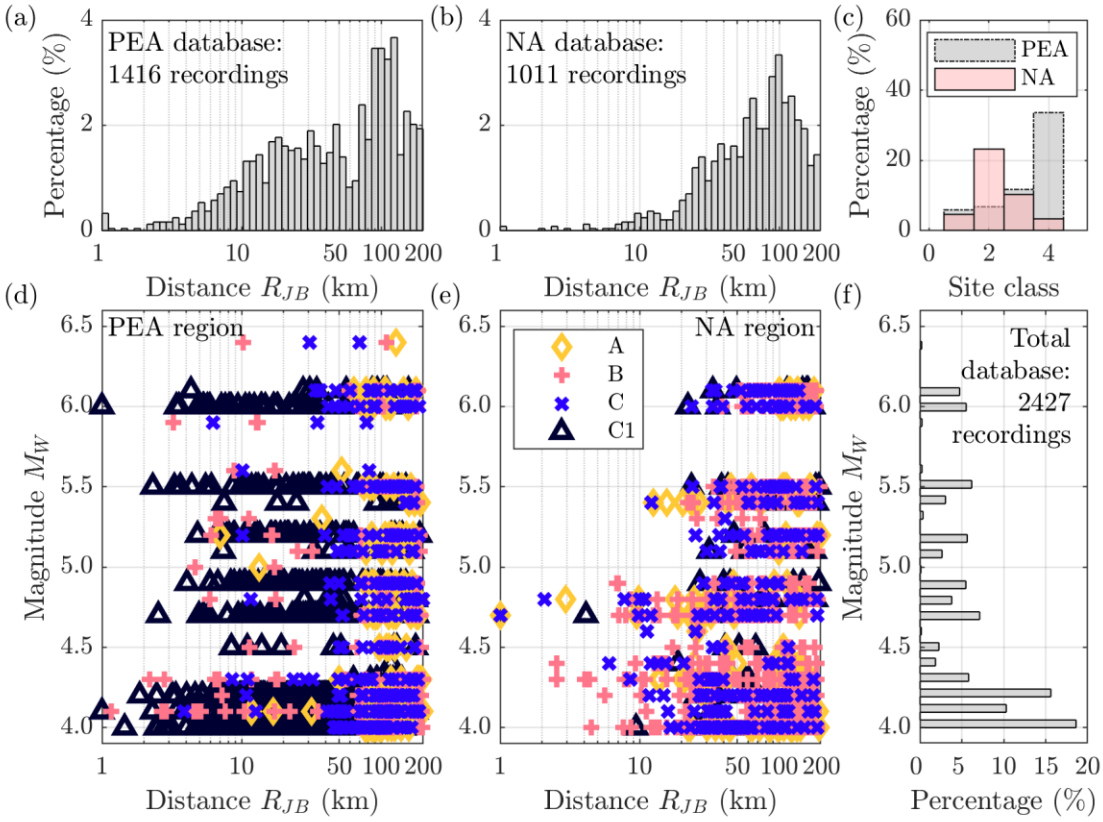

Figure 2 (a, b) R_{JB} histograms of PEA and NA datasets, respectively; (c) site classification histogram; (d, e) M_W-R_{JB} scatter plots of PEA and NA datasets, respectively; and (f) M_W histogram of the considered records. The percentage is calculated with respect to the total size of the dataset.

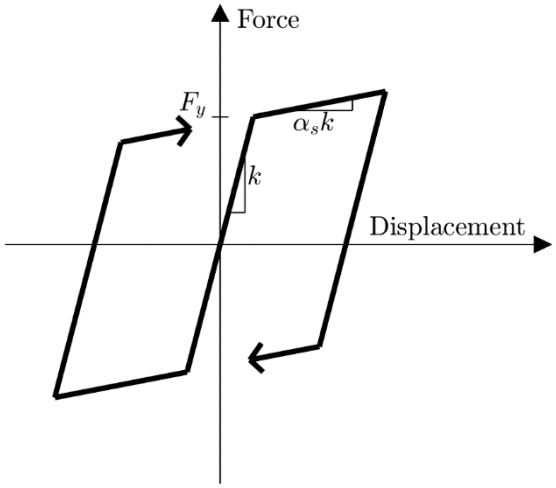

668

669 Figure 3 Hysteretic model considered for the inelastic SDoF oscillators

670

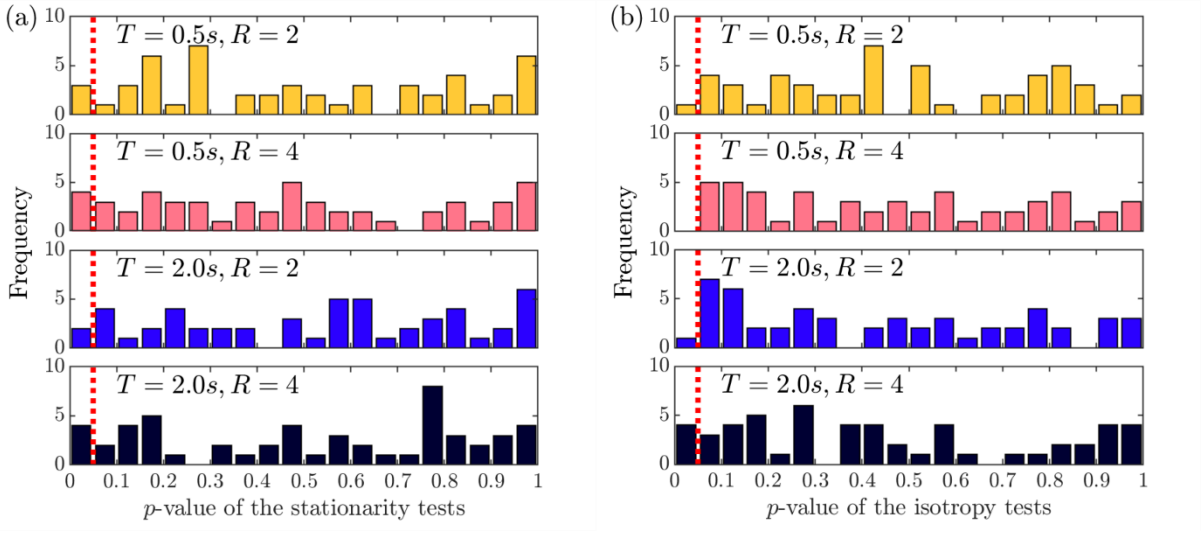

671

672 Figure 4 p-values of the (a) stationarity; and (b) isotropy hypothesis tests. Values larger than

673 0.05 (denoted by the dashed line) indicate the appropriateness of stationarity and isotropy

674 assumptions.

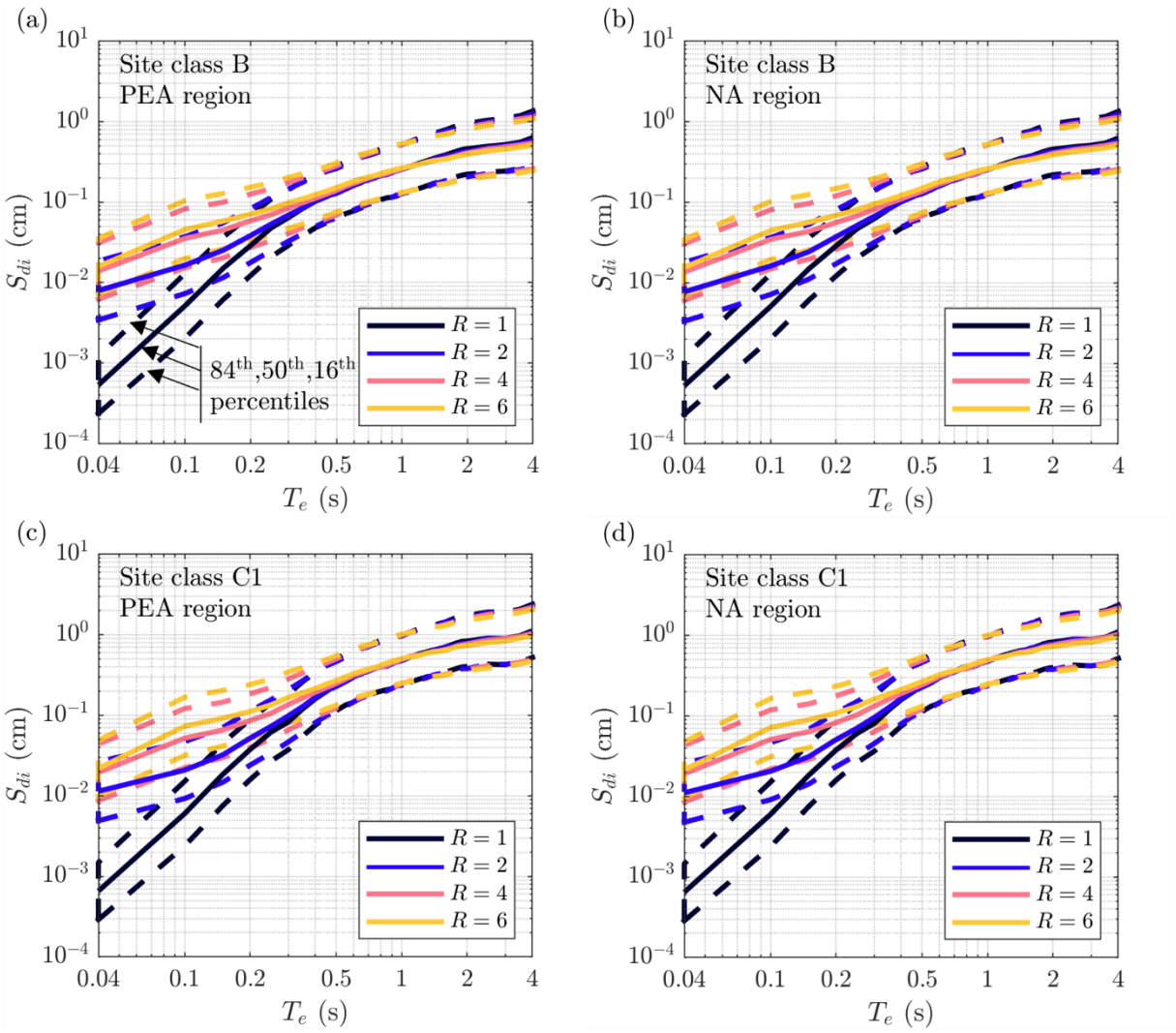

675

676 Figure 5 S_{di} spectra for a $M_W = 6.0$ thrust event at $R_{JB} = 60$ km and for site class (a,b) B

677 and (c,d) C1 in the (a,c) Po Plain and Eastern Alps (PEA) and (b,d) Northern Apennines (NA)

678 regions.

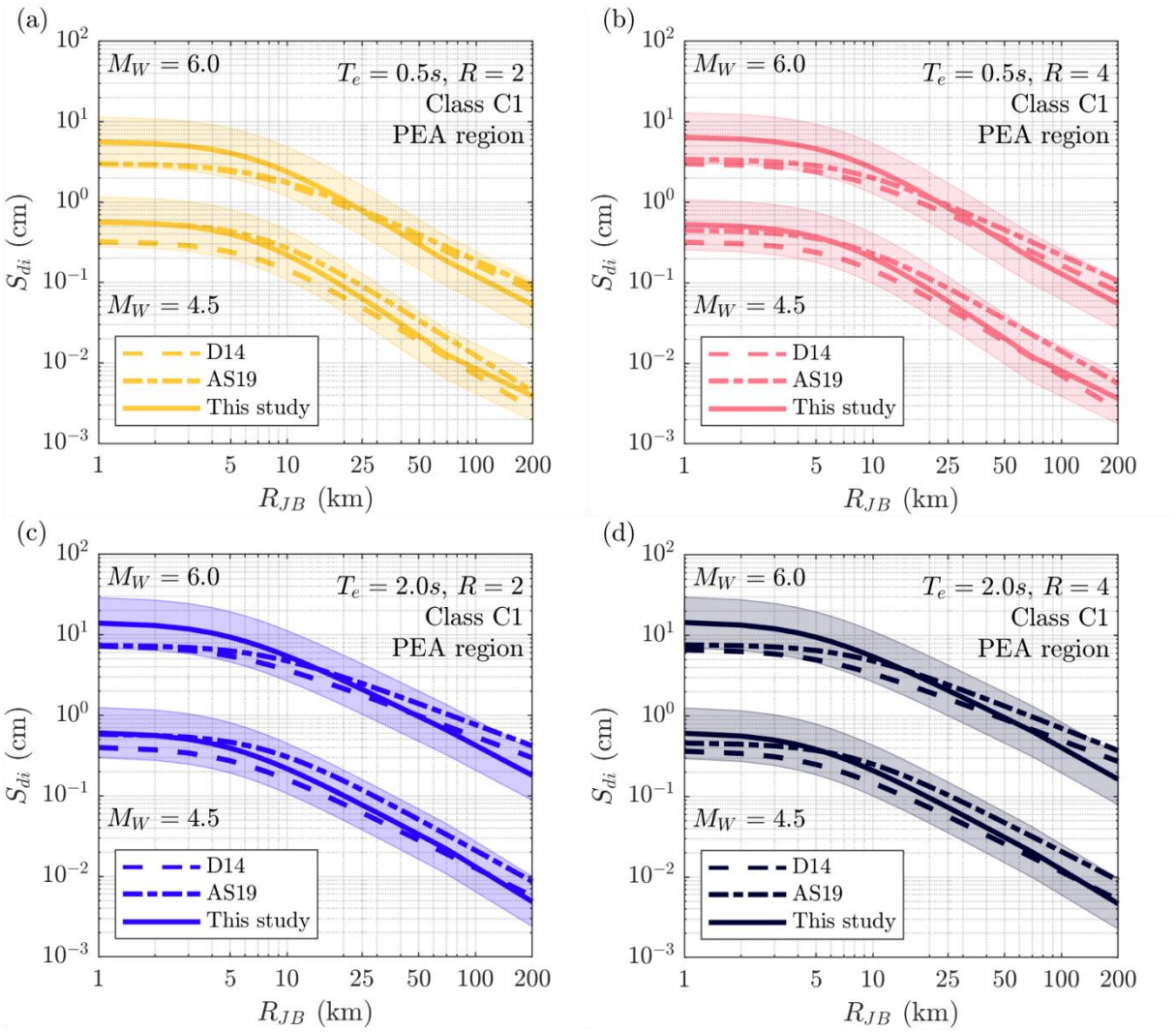

Figure 6 Median S_{di} at site class C1 in the PEA region for M_W 4.5 and 6.0 thrust events compared with the median estimates from De Luca *et al.* (2014a, 2014b) (D14) and Akkar and Sandıkkaya (2019) (AS19) models. The shaded band depicts the 84th-16th percentile of the developed model.

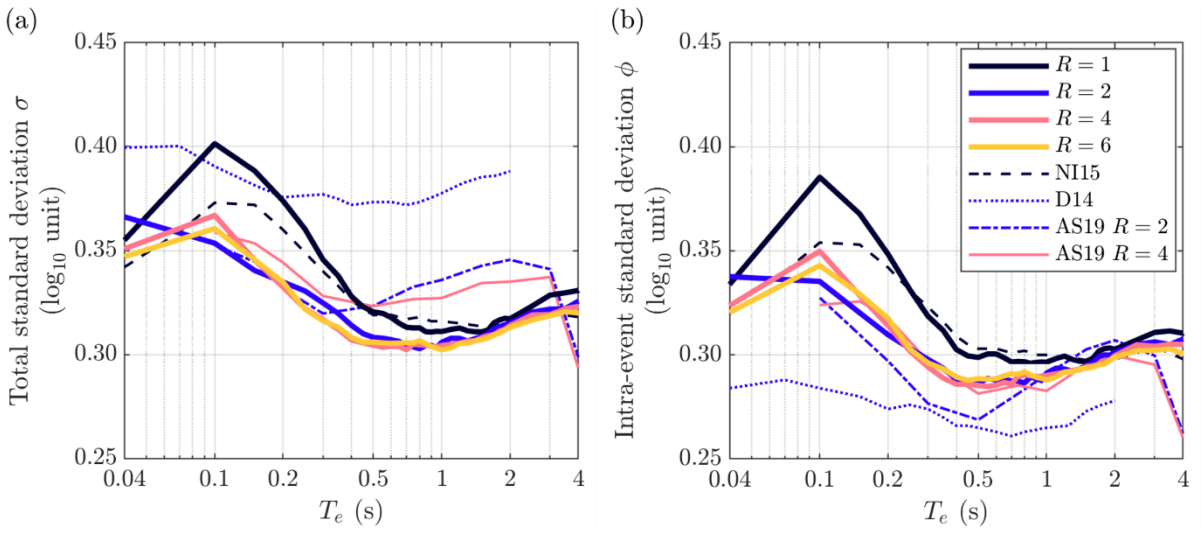

684

685 Figure 7 (a) Total and (b) intra-event standard deviations of S_{di} at four inelasticity levels

686 compared with the Lanzano *et al.* (2016) (NI15), De Luca *et al*. (2014a, 2014b) (D14), and

687 Akkar and Sandıkkaya (2019) (AS19) models.

688

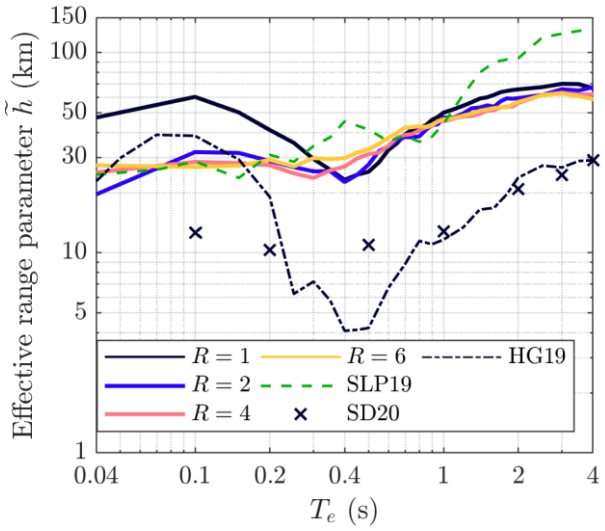

689

690 Figure 8 The effective range parameter of S_{di} for R=1-6 compared with the Sgobba *et al.*

691 (2019) (SLP19), Huang and Galasso (2019) (HG19), and Schiappapietra and Douglas (2020)

692 (SD20) models for the elastic spectral ordinates.

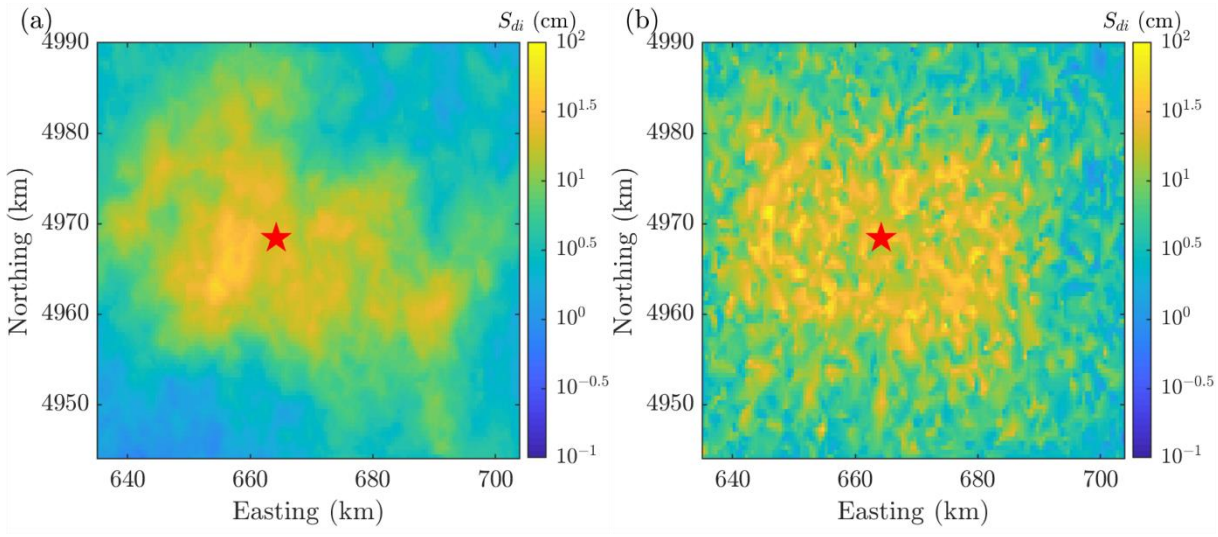

693

694 Figure 9 A realization of S_{di} for $T_e = 2.0s$ and $R = 2$ system subject to a $M_W 6.0$ event

695 illustrated by the star ★using the developed: (a) with and (b) without spatial correlation

696 consideration.

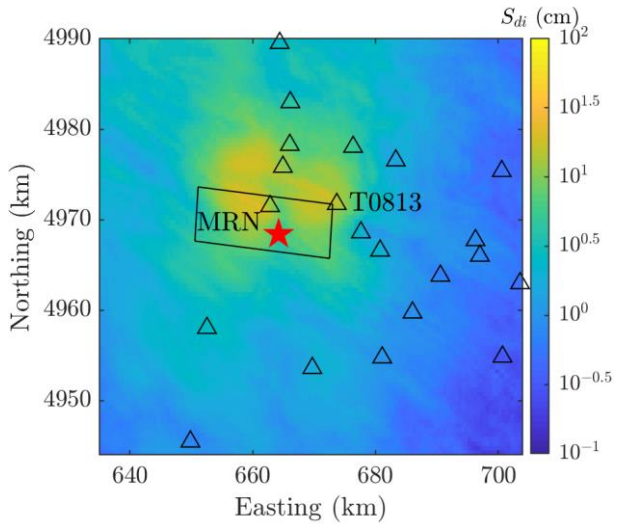

697

698 Figure 10 S_{di} for a $T_e = 2.0s$ $R = 2$ system subjected to the simulated ground motions of

699 the $M_W 6.0$ Emilia-Romagna earthquake (Paolucci *et al.*, 2015). The epicenter and stations

700 which recorded the event are shown by a star ★ and triangles Δ, respectively. The square denotes

701 the ruptured fault plane projected on the ground surface.

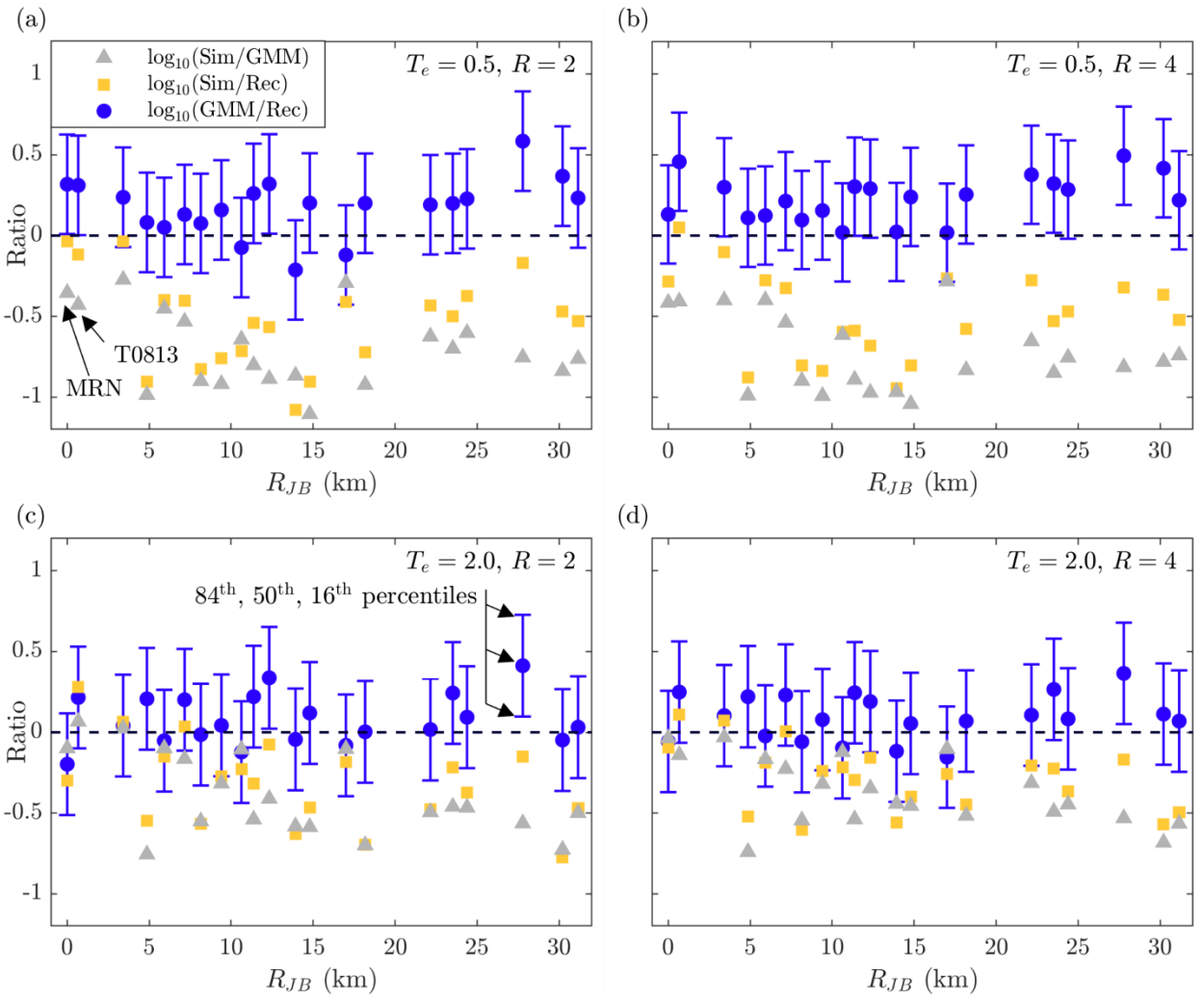

Figure 11 The ratio of S_{di} from the simulation and developed GMM with respect to each other and the S_{di} from recorded ground-motions for T_e=0.5 and 2.0 s and R= 2.0 and 4.